Preprint typeset using LaTeX style emulateapj v. 12/16/11

GAMMA-RAY ECLIPSES AND ORBITAL MODULATION TRANSITIONS IN THE CANDIDATE REDBACK 4FGL J1702.7-5655

R. H. D. Corbet[1,2], L. Chomiuk[3], J. B. Coley[4], G. Dubus[5], P. G. Edwards[6], N. Islam[1], V. A. McBride[7], J. Stevens[6], J. Strader[3], S. J. Swihart[8], L. J. Townsend[9]

Submitted: Dec 19, 2021

ABSTRACT

Observations with the Fermi Large Area Telescope (LAT) of the gamma-ray source 4FGL J1702.7−5655, previously classified as a candidate millisecond pulsar, show highly-significant modulation at a period of 0.2438033 days (∼5.85 hours). Further examination of the folded light curve indicates the presence of narrow eclipses, suggesting this is a redback binary system. An examination of the long-term properties of the modulation over 13 years of LAT observations indicates that the orbital modulation of the gamma-rays changed from a simple eclipse before early 2013, to a broader, more easily detected, quasi-sinusoidal modulation. In addition, the time of the eclipse shifts to ∼0.05 later in phase. This change in the orbital modulation properties is, however, not accompanied by a significant overall change in gamma-ray flux or spectrum. The quasi-sinusoidal component peaks ∼0.5 out of phase with the eclipse, which would indicate inferior conjunction of the compact object in the system. Swift X-ray Telescope observations reveal a possible X-ray counterpart within the LAT error ellipse. However, radio observations obtained with the Australia Telescope Compact Array do not detect a source in the region. 4FGL J1702.7−5655 appears to have changed its state in 2013, perhaps related to changes in the intrabinary shock in the system. We discuss how the properties of 4FGL J1702.7−5655 compare to other binary millisecond pulsars that have exhibited orbital modulation in gamma rays.

Keywords: stars: individual (CXOU J053600.0-673507, 4FGL J1702.7−5655) — stars: neutron — gamma-rays: stars

1. INTRODUCTION

1.1. *Binary Millisecond Pulsars*

Millisecond pulsars (MSPs) are pulsars with short pulse periods, but which are apparently old as indicated by their slow spin-down rates. They are believed to be descended from low-mass X-ray binaries (LMXBs). Some MSPs are found in "spider" binaries with a low-mass companion that is being ablated by the wind from the pulsar (e.g. Roberts 2013). The spider binaries are generally divided into black widow systems, in which the companion is very low mass and may be degenerate, and redbacks where the companion is a near main-sequence star. An intrabinary shock (IBS) is thought to exist between the winds from the pulsar and its companion, and this can be the site of X-ray and radio emission (e.g. Gentile et al. 2014; Roberts et al. 2014; Kandel et al. 2019; van der Merwe et al. 2020). Orbitally modulated emission is commonly seen both in X-rays, associated with accelerated particles in the IBS, and at radio wavelengths where eclipses can be caused by scattering in dense ionized material. The optical emission is dominated by the light from the pulsar's companion, and this is generally modulated on the orbital period due to both gravitational ellipsoidal distortion and heating of the face of the companion that is facing the pulsar (e.g. Breton et al. 2013).

Several redbacks have been seen to change between states in which the primary power source is the rotational energy of the neutron star, and those in which accretion is occurring from the companion, and it becomes an LMXB. These are termed "transitional millisecond pulsars" (tMSPs, e.g. Papitto & de Martino 2020). In tMSPs three states are generally identified: (i) a pulsar state where the pulsar is the power source in the system and accretion is not occurring; (ii) accretion states where accretion onto the surface of the neutron star occurs; (iii) a sub-luminous disk state where there can be rapid changes on timescales as short as ∼10 s between high and low X-ray flux levels, with intermittent flares also present. Gamma-ray brightening may accompany a change from the rotation-powered state to the subluminous state.

The Large Area Telescope (LAT) on board the Fermi Gamma-ray Space Telescope has been surveying the gamma-ray sky above 100 MeV since 2008, and it

[1] University of Maryland, Baltimore County, and X-ray Astrophysics Laboratory, Code 662 NASA Goddard Space Flight Center, Greenbelt Rd., MD 20771, USA.
[2] Maryland Institute College of Art, 1300 W Mt Royal Ave, Baltimore, MD 21217, USA.
[3] Department of Physics and Astronomy, Michigan State University, East Lansing, MI 48824, USA.
[4] Department of Physics and Astronomy, Howard University, Washington, DC 20059, USA. CRESST/Code 661 Astroparticle Physics Laboratory, NASA Goddard Space Flight Center, Greenbelt Rd., MD 20771, USA.
[5] Institut de Planétologie et d'Astrophysique de Grenoble, Univ. Grenoble Alpes, CNRS, F-38000 Grenoble, France.
[6] Commonwealth Scientific and Industrial Research Organisation Astronomy and Space Science, PO Box 76, Epping, New South Wales 1710, Australia.
[7] Department of Astronomy, University of Cape Town, Private Bag X3, Rondebosch, 7701, South Africa.
[8] National Research Council Research Associate, National Academy of Sciences, Washington, DC 20001, USA,
resident at Naval Research Laboratory, Washington, DC 20375, USA.
[9] South African Astronomical Observatory, PO Box 9, Observatory, 7935, South Africa.

has now identified more than 5000 sources. Of these, a significant number (> 260; e.g. Grießmeier et al. 2021) have been identified as pulsars, with a large fraction being MSPs[10]. Detection of periodic orbital modulation in MSPs at gamma-ray energies is relatively uncommon, compared to that at other energies. 4FGL J0427.8−6704 (3FGL J0427.9−6704) was previously found to exhibit eclipses in gamma rays, X-rays, and the optical (Strader et al. 2016; Kennedy et al. 2020) at a period of ∼0.366 days. More recently, Clark et al. (2021b) found what they describe as "subtle" gamma-ray eclipses in four systems: 4FGL J1048.6+2340 (PSR J1048+2339), 4FGL J1816.5+4510 (PSR J1816+4510), 4FGL J2129.8−0428 (PSR J2129-0429), and PSR B1957+20. The detection of these eclipses exploited orbital ephemerides obtained from radio and gamma-ray pulse timing, which give both the orbital period and the epoch of expected eclipse.

We have been conducting a search for previously unrecognized gamma-ray emitting binaries in the Fermi-LAT catalogs by searching for periodic modulation of the LAT flux. This has enabled us to detect several high-mass systems (Corbet et al. 2019, and references therein). Here we present the detection of strong periodic gamma-ray modulation in LAT observations of the candidate redback system 4FGL J1702.7−5655. We find that it exhibits periodic dips in its light curve that are consistent with eclipses in a redback system. In addition, an investigation of the multi-year behavior indicate a change in modulation properties from just a periodic dip to quasi-sinusoidal modulation together with a dip at a slightly later phase. We also searched for X-ray and radio counterparts of 4FGL J1702.7−5655 using the Swift X-ray Telescope (XRT) and the Australia Telescope Compact Array (ATCA) respectively, and identify a possible X-ray counterpart although no counterpart is detected at radio wavelengths. We compare the gamma-ray modulation in 4FGL J1702.7−5655 to that in other systems, and speculate on the cause of the change in orbital modulation. Unless otherwise noted, uncertainties are given at the 1σ level.

1.2. *Previous Observations of 4FGL J1702.7−5655*

4FGL J1702.7−5655 is in the fourth LAT catalog (Abdollahi et al. 2020) and counterparts were also present in the third catalog (3FGL J1702.8−5656; Acero et al. 2015), the LAT eight year source list[11] (FL8Y J1702.7-5654), the second catalog (2FGL J1702.5-5654; Nolan et al. 2012), and the first catalog (1FGL J1702.4-5653; Abdo et al. 2010). It may also be associated with the AGILE gamma-ray source 2AGL J1703−5705 (Bulgarelli et al. 2019). Saz Parkinson et al. (2016) undertook a classification of sources in the 3FGL catalog into pulsars and active galactic nuclei - the two main categories of identified LAT sources. From this analysis they found that 3FGL J1702.8−5656 was most likely to be a millisecond pulsar. 3FGL J1702.8−5656 was included in a search for gamma-ray pulsations from Fermi LAT observations for frequencies < 1520 Hz by Clark et al. (2017) and Wu et al. (2018), but none were reported. In addition, 3FGL J1702.8−5656 was included in a search for radio pulsations using the Parkes telescope by Camilo et al. (2015) made with 125μs time resolution and none were found from this source.

2. OBSERVATIONS AND ANALYSIS

2.1. *Gamma-ray Observations and Analysis*

The Fermi LAT (Atwood et al. 2009; Ajello et al. 2021) is a pair conversion telescope sensitive to gamma-ray photons with energies between ∼20 MeV to > 300 GeV. The LAT data used in this paper were obtained between 2008 August 4 and 2021 August 19 (MJD 54,682 to 59,445). During this time, Fermi was primarily operated in a sky survey mode. Until 2018 the LAT pointing position was alternately rocked away from the zenith to the orbit north for one spacecraft orbit, then towards the orbit south for one orbit. In this way, the entire sky was observed every two spacecraft orbits, approximately every three hours. After a failure of the drive for one solar array, changes were made to the sky survey profiles, but coverage of the entire sky was maintained in the long term (Ajello et al. 2021).

Our search for new gamma-ray binaries followed similar procedures to those described in Corbet et al. (2019). For LAT analysis we used the `fermitools` version `1.0.1` with the updated Pass 8 LAT data files ("P8R3", Bruel et al. 2018) and the weekly photon files provided by the Fermi Science Support Center which include precomputed diffuse response columns. Light curves covering an energy range of 100 MeV to 500 GeV were created for all 4FGL DR2 sources using time bins of 500 s. Times when sources were closer than 5 degrees to the Sun were excluded, but no filtering was applied for distance from the Moon. The light curves were obtained using a variant of aperture photometry where we estimate the probability "p" that each photon comes from a source of interest and sum these probabilities (e.g. Kerr 2011; Fermi LAT Collaboration et al. 2012; Kerr 2019). To facilitate this, model files were created for each source using `make4FGLxml` including sources from the 4FGL DR2 catalog within a 10 degree radius from the source. Photon probabilities were calculated using `gtsrcprob` and then summed for a 3 degree radius aperture centered on each source. We used `gtbin` to create the initial light curves, but then replaced the integer `COUNTS` column with a floating point `RCOUNTS` column containing the calculated summed probabilities. The exposure for each time bin was calculated using `gtexposure` to obtain the probability weighted rate in units of $\mathrm{p\,ph\,cm^{-2}\,s^{-1}}$ and times were corrected to the Solar System barycenter with `gtexposure`. We note that although the use of "probability photometry" generally increases the signal-to-noise of the light curves, it affects the photometric properties as probabilities are based on a constant source brightness. Thus, when a source is brighter than the model predicts, the probability of a photon coming from the source is underestimated, and, when the source is fainter than the model prediction, the probability is overestimated (e.g. Kerr 2019). This results in a reduction of the apparent amplitude of any variability.

Power spectra of these LAT light curves were calculated using Discrete Fourier Transforms (DFT), weighting each data point's contribution by its relative expo-

[10] https://confluence.slac.stanford.edu/display/GLAMCOG/Public+List+of+LAT-Detected+Gamma-Ray+Pulsars

[11] https://fermi.gsfc.nasa.gov/ssc/data/access/lat/fl8y/

sure after first subtracting the mean count rate. This is beneficial because of the substantial exposure changes from time bin to time bin. We note that while the time bins produced by `gtbin` are evenly spaced, although with gaps, this is no longer the case after the barycenter correction. However, even spacing is not required for calculation of a DFT. The use of weighting does not, however, change the intrinsic statistical properties of the power spectrum (Zechmeister & Kürster 2009; VanderPlas 2018) and the powers are expected to be distributed given by an exponential probability function. We normalize the computed powers to have a average power of unity. The power spectra cover a period range from 0.05 days (1.2 hrs) to the length of the light curve, i.e. ∼4762 days, giving ∼95,246 independent frequencies. The power spectra were oversampled by a factor of 5 compared to the nominal resolution, which we take to be the inverse of the length of the light curve ("T") (e.g. VanderPlas 2018, and references therein), i.e. $\sim 1/4762$ days^{-1}. For the strongest peak in each power spectrum the False Alarm Probability (FAP, Scargle 1982), the estimated probability of a signal reaching a power level by chance assuming white noise, was calculated.

$$FAP = 1 - [1 - \exp(-r)]^N \tag{1}$$

where r is the normalized height of the peak power, and N is the number of independent frequencies. This calculation of the FAP takes into account the number of independent frequencies searched, correcting for the oversampling of the power spectra, but does not include the effect of searching for periodicity in multiple sources. In the case where we are examining a power spectrum for the presence of a previously reported periodicity with a small uncertainty, N may be set equal to unity, and hence a lower amplitude signal can give a smaller FAP than the case for a "blind" search. The uncertainty in the frequency of a candidate modulation that is detected can be calculated using the derivation of Horne & Baliunas (1986) and as also discussed by Levine et al. (2011):

$$\delta f = \frac{3}{8}\frac{1}{T\sqrt{r}} \tag{2}$$

Since the period, P, $= 1/f$, propagation of errors yields:

$$\begin{aligned} \frac{\delta f}{f} &= \frac{\delta P}{P} \\ \Rightarrow \delta P &= \frac{3}{8}\frac{P^2}{T\sqrt{r}} \end{aligned} \tag{3}$$

Hence, the fractional uncertainty of the frequency and period

$$\frac{\delta f}{f} = \frac{\delta P}{P} \propto f^{-1} \tag{4}$$

i.e. the fractional uncertainty on the measurement of the frequency and period of a detected modulation is smaller for short periods/high frequencies than long periods/low frequencies. In addition, the degree to which a frequency can be measured more precisely than the intrinsic Fourier resolution, $\pm 1/(2T)$, scales as the square root of the normalized peak height.

In our photometric analyses the background is not fitted for each time bin, and artifact signals can be seen at several periods including Fermi's ∼90 minute orbital period, the survey period at twice this, one day, the Moon's 27.3 day sidereal period, the 53 day precession period of the Fermi satellite's orbit, and one quarter of a year related to the shape of the LAT PSF[12].

2.2. *X-ray Observations and Analysis*

The Swift-XRT (Burrows et al. 2005) is a Wolter I X-ray imaging telescope sensitive to X-rays ranging from 0.3 to 10 keV. The location of 4FGL J1702.7−5655 had previously been observed for 4ks with the XRT under the program of Stroh & Falcone (2013) to monitor unassociated LAT sources. As no source was clearly detected in these observations, additional observations were obtained under the Swift TOO program to acquire a total of ∼17.5 ks of exposure. All observations were made in photon counting (PC) mode. The log of XRT observations is given in Table 1. We analyzed the existing and new data sets together using the online tools provided at the University of Leicester (Goad et al. 2007; Evans et al. 2009) to extract an image, and for source detection and position determination[13].

2.3. *Radio Observations and Analysis*

Radio observations covering the location of 4FGL J1702.7−5655 were obtained using ATCA (Wilson et al. 2011) between December 2020 to November 2021 (MJD 59208 to 59540, see Table 2), i.e. during Part 2 of the gamma-ray light curve (Section 3.1), with observations centered at 2.1, 5.5 and 9.0 GHz, with 2 GHz bandwidths for all three bands. The ATCA, which consists of six 22 m-diameter antennas, was in several different array configurations over this period, with the more compact arrays somewhat more sensitive to the bright extended emission in the vicinity. Details of the array configurations are given in Table 2. Observations were reduced following standard procedures in Miriad (Sault et al. 1995). PKS 1657-56 was used as phase calibrator and PKS 1934-638 was used as a primary flux density calibrator for all observations.

3. RESULTS

3.1. *Gamma-ray Results*

From our examination of the power spectra of the LAT light curves of all 4FGL DR2 sources we noted significant modulation from 4FGL J1702.7−5655. The power spectrum of the LAT light curve is shown in Fig. 1. There is a prominent peak near a period of 0.24 days at a height of 25.7 times the mean power level and the associated FAP is 7×10^{-7}. To investigate the frequency dependence of the continuum power we performed a fit of the logarithm of the power as a function of the logarithm of the frequency as advocated by Vaughan (2005). From this we find that the continuum is very flat with only a hint of a small increase at lower frequencies/longer periods with $Power \propto f^{-4(\pm2)\times10^{-3}}$. We note that the apparent increase in power at shorter periods in Fig. 1 is not real and is due to the logarithmic scale which prevents individual points being discerned at high frequencies,f and only the statistical envelope being visible.

[12] http://fermi.gsfc.nasa.gov/ssc/data/analysis/LAT_caveats_temporal.html
[13] https://www.swift.ac.uk/user_objects/

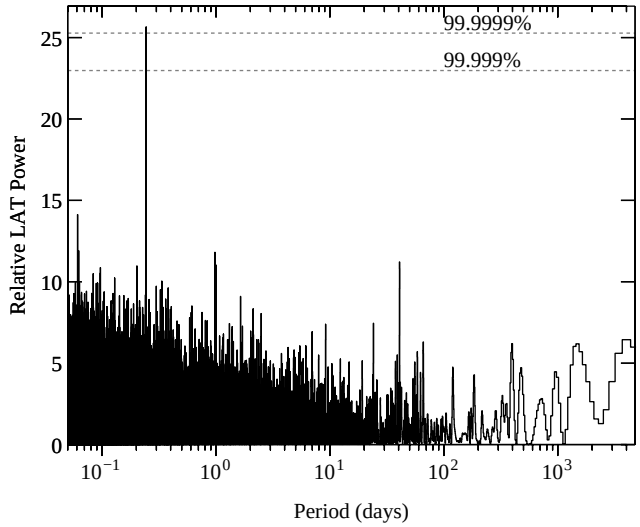

Figure 1. Power spectrum of the Fermi LAT probability-weighted aperture photometry light curve of 4FGL J1702.7−5655.

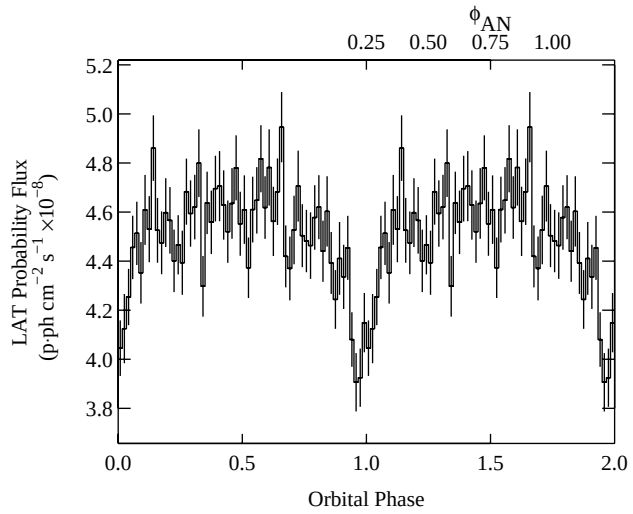

Figure 2. Fermi LAT probability-weighted aperture photometry light curve of 4FGL J1702.7−5655 folded on the proposed orbital period. The bottom X-axis uses eclipse center to define orbital phase zero. The upper labels show the predicted orbital phases with time of ascending node defining zero.

No obvious peaks are seen at the second, third, or fourth harmonics of this. The period is determined to be 0.2438033(11) days using the formulation of Horne & Baliunas (1986), i.e. 5.851279(26) hours. Since this would be a typical orbital period for a binary MSP (e.g. Papitto & de Martino 2020), we assume that this is indeed the orbital period of 4FGL J1702.7−5655. The probability-weighted aperture photometry LAT light curve folded on the 0.24 day period is shown in Fig. 2. This shows a relatively sharp dip that is strongly suggestive of the presence of an eclipse, implying that the system is observed at a high inclination angle.

In order to search for any long-term changes in the orbital modulation we obtained a dynamic power spectrum of the probability-weighted aperture photometry LAT light curve. We calculated power spectra for light curves of length 650 days, with offsets of 50 days between

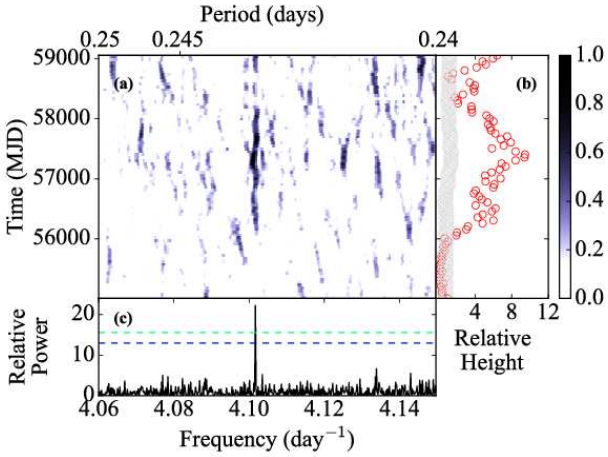

Figure 3. (a) Dynamic power spectrum of the probability-weighted aperture photometry LAT light curve of 4FGL J1702.7−5655. (b) Relative peak at the orbital period to the mean power of the values shown in panel (a). (c) Coherent power spectrum of the entire light curve.

successive light curves. The results of this are shown in Fig. 3 and it suggests that the orbital modulation was less apparent during earlier time ranges. To explore this further, we investigated the growth in relative height of the peak in the power spectrum as a function of time. For a persistent coherent signal with constant background and no other changes, the relative power should grow linearly with time as the amplitude noise decreases as the square root of the observation time. In Fig. 5 we plot the relative height of the orbital peak using light curves that all end at the same time (MJD 59,445) but have different start dates. From this, it can be seen that as the start date is moved earlier, the relative strength of the peak initially grows as the light curve length increases. However, for light curve start times earlier than ∼3100 days before the end of the light curve (i.e. start times earlier than ∼MJD 56,345 = 2013-02-22) a plateau appears with little overall increase in relative power.

To investigate this in more detail we calculated power spectra for the LAT light curve divided into two sections before and after MJD 56,345. These are shown in Fig. 7 and it can be seen that there is no significant orbital peak in the power spectrum for the earlier light curve segment ("Part 1") while it is strongly detected for the later segment ("Part 2"). We then folded the light curve on the orbital period using data from these two time ranges and these are shown in Fig. 4. From these it can be seen that the time of the minimum is shifted to the right and is broader for Part 2 compared to Part 1. In

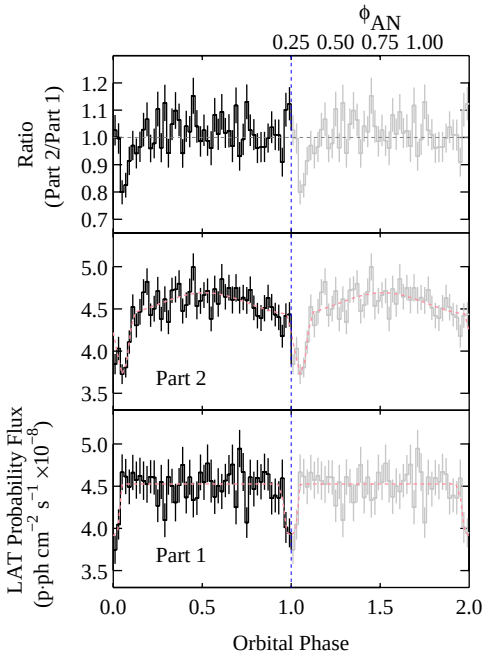

Figure 4. The probability-weighted aperture photometry LAT light curve of 4FGL J1702.7−5655 obtained for time ranges of MJD 54,682 - 56,345 (bottom) and 56,345 - 59,445 (middle) folded on the orbital period. The top panel shows the ratio of the count rate in the second part to the first part. The dashed pink lines in the bottom two panels indicate the fits made to the unfolded light curves, the parameters are given in Table 3. For clarity, for all panels two identical cycles are plotted with the second cycle plotted in gray. The bottom X-axis uses eclipse center to define orbital phase zero. The upper labels show the predicted orbital phases with time of ascending node defining zero.

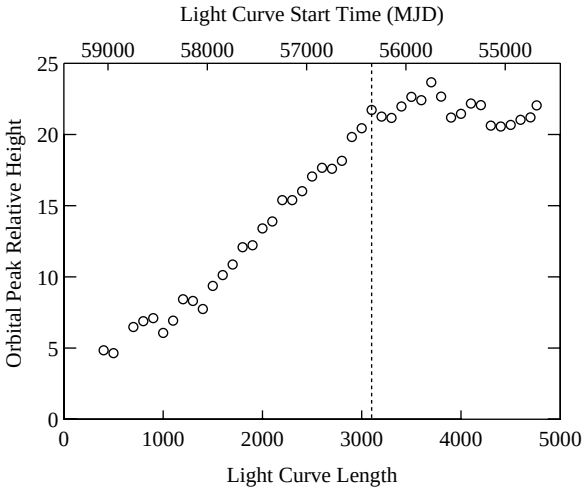

Figure 5. Relative height of the orbital peak in the power spectrum of the probability-weighted aperture photometry LAT light curve of 4FGL J1702.7−5655. All light curves have the same end date of MJD 54,682, and the start date, shown in the top axis, is changed in the analysis.

Part 2 the weighted count rate outside the eclipse is also slightly higher as indicated by the upper panel of Fig. 4 which shows the ratio of the two folded light curves.

We note that we cannot determine the exact time of the change in orbital modulation due to the long integration times required to detect the modulation and changes in it. We also investigated the effect on the power spectrum dividing the light curve into halves with a 600 day earlier split (MJD 55,745) where the relative peak in Fig. 5 is at its maximum. In this case, we find that the *absolute* power for Part 2 is reduced by ∼12% compared to dividing the light curve at MJD 56,345 (Fig. 7). Thus, any sinusoidal orbital modulation between MJD 55,745 to 56,345 would be at a lower amplitude.

In order to search for other long-term changes in the gamma-ray properties that, for example, could be an indication of a state change in a tMSP we calculated a light curve using a binned likelihood analysis. We performed likelihood fitting using time bins of 200 days, an energy range of 100 MeV to 500 GeV, a region of interest of 10 degrees, and the spectral parameters for 4FGL J1702.7−5655 were allowed to float, while spectral values for other sources in the region were held fixed. The spectral model used for 4FGL J1702.7−5655 in the 4FGL catalog is a log normal function (`LogParabola`), i.e.

$$\frac{dN}{dE} = K \left(\frac{E}{E_0}\right)^{-\alpha-\beta\, log_e(E/E_0)} \quad (5)$$

This model is used in the LAT catalogs for all sources with significantly curved spectra. The resulting light curve is shown in Fig. 6 and the approximate time where the orbital modulation changed to become prominent in the light curve is marked. Although the light curve is formally inconsistent with the hypothesis of being constant ($\chi^2_\nu = 3.1$), we do not see any clear changes in the flux level or spectral parameters associated with the change in the orbital profile. The mean flux before the division is 2.5 ± 0.3 $\times 10^{-8}$ ph cm^{-2} s^{-1} (1.8 ± 0.2 $\times 10^{-11}$ erg cm^{-2} s^{-1}), while after it is 2.9 ± 0.3 $\times 10^{-8}$ ph cm^{-2} s^{-1} (2.1 ± 0.2 $\times 10^{-11}$ erg cm^{-2} s^{-1}). For α, the values before and after are 2.36 ± 0.03 and 2.38 ± 0.3, while for β they are 0.30 ± 0.05 and 0.30 ± 0.04, respectively.

In order to characterize the orbital modulation we fitted periodic functions to the *unfolded* weighted aperture photometry light curves. Since the eclipse has a relatively short duration, we extracted light curves with 100 s time bins, i.e. ∼0.005 of the orbital period. We fitted the two parts of the light curve separately. For Part 1 we used an eclipse profile with constant fluxes outside and inside the eclipse, and linear transitions between these, with independent durations for the eclipse ingress and egress. The profile is defined in terms of time of orbital period and eclipse center, which we define as $\phi = 0$, the phase of the start of eclipse ingress ($\phi_{\rm ing}$), the phase of the end of egress ($\phi_{\rm egr}$), the total duration of the eclipse minimum (Δ), flux outside eclipse ($F_{\rm unecl}$), and flux during eclipse totality ($F_{\rm ecl}$). In the fits $\phi_{\rm ing}$ and $\phi_{\rm egr}$ were constrained to occur before and after the phases of eclipse totality respectively. Similarly to the computation of the power spectra, the data points were weighted by their relative exposures.

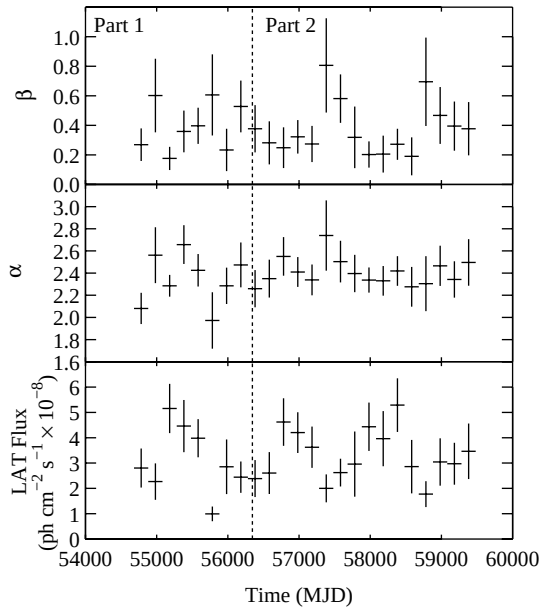

Figure 6. Long-term Fermi LAT light curve of 4FGL J1702.7−5655 obtained from a maximum likelihood analysis. The energy range is 100 MeV to 500 GeV and the spectral parameters are for the logParabola model used in the 4FGL catalog. The dashed line shows the division between Part 1 and Part 2 at MJD 56,345.

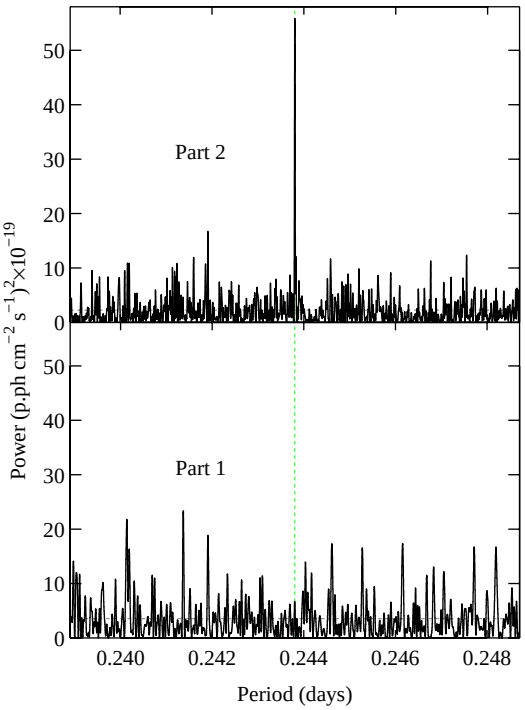

Figure 7. Power spectra of the probability-weighted aperture photometry LAT light curve of 4FGL J1702.7−5655 obtained for time ranges of MJD 54,682 - 56,345 (bottom) and 56,345 - 59,445 (top). The period ranges are centered on the presumed orbital period marked with the vertical dashed green line. The mean power level for each panel is marked with a dashed horizontal gray line. Note that the y axis is in units of absolute, rather than relative, power and that the same range is plotted for both panels.

$$F = \begin{cases} F_{\rm unecl}, & \phi_{\rm egr} \le \phi \le \phi_{\rm ing} \\ F_{\rm unecl} + (\frac{(F_{\rm ecl}-F_{\rm unecl})(\phi-\phi_{\rm ing})}{(1-(\frac{\Delta}{2})-\phi_{\rm ing})}), & \phi_{\rm ing} \le \phi \le (1-(\frac{\Delta}{2})) \\ F_{\rm ecl}, & \phi \ge (1-(\frac{\Delta}{2})); \phi \le \Delta/2 \\ F_{\rm ecl} + (\frac{(F_{\rm unecl}-F_{\rm ecl})(\phi-(\frac{\Delta}{2}))}{(\phi_{\rm egr}-(\frac{\Delta}{2}))}), & (\frac{\Delta}{2}) \le \phi \le \phi_{\rm egr} \end{cases} \quad (6)$$

Derived from these fitted parameters are the total eclipse phase duration from eclipse ingress start to egress end (1 + $\phi_{\rm egr}$ - $\phi_{\rm ing}$), the phase duration of the ingress (1 - ($\frac{\Delta}{2}$) - $\phi_{\rm ing}$), and the phase duration of the egress ($\phi_{\rm egr}$ - ($\frac{\Delta}{2}$)).

For the fit to the unfolded Part 2 light curve we used a sum of the same eclipse model together with an additional sine wave component. For both fits we held the orbital period at the value determined from the power spectrum of Part 2. If we allowed the orbital period to be free we found that this resulted in unstable fits.

The parameters from the fits to both sections of the light curve are given in Table 3. The parameter 1 σ uncertainties are derived from the intervals that give $\chi^2_{min} + 1$ (Lampton et al. 1976).

We use the center of the eclipse for the Part 1 light curve to define phase zero and find this to be MJD 57000.168, with an uncertainty of 0.004 days (uncertainty of 0.017 in phase). This would correspond to superior conjunction of a pulsar, assuming that is indeed the source of the gamma-rays and it is being eclipsed by its companion. For a pulse timing circular orbit with phase 0 defined as the ascending node, this would correspond to a phase (ϕ_{AN}) of 0.25. The Part 1 eclipse width from ingress start to egress end is 0.110 ± 0.038 in phase. The ingress and egress durations are not well defined and are consistent with 0.

For the Part 2 light curve, the center of the eclipse minimum is shifted to a slightly later time by 0.014 ± 0.005 days. i.e. our fits indicate that the centers of the two eclipses differ 0.059 ± 0.020 in phase. The semi-amplitude of the sine wave component is 0.127 ± 0.034 $\times 10^{-8}$ p ph cm^{-2} s^{-1}, equivalent to a fractional semi-amplitude of 2.8 ± 0.7 %. This corresponds to a power of 16 ± 9 $\times 10^{-19}$ (p.ph cm^{-2} s^{-1})^2. The measured power for the orbital modulation in Part 2 is ∼55 $\times 10^{-19}$ (p.ph cm^{-2} s^{-1})^2 (Fig. 7) and so, at least in this representation of the light curve components, the eclipse feature also contributes to the observed signal in the power spectrum. This may be due to the eclipse, which occurs at the minimum of the sine component, becoming broader. We note, however, that this mathematical deconvolution does not necessarily relate to two astrophysically distinct components.

We next investigated the orbital gamma-ray modulation by performing likelihood fits to binary phase-resolved LAT data. We divided the light curve into 50 phase bins. Our analysis was similar to that for the long-term light curve, except that we also held the spectral parameters of 4FGL J1702.7−5655 fixed and only allowed its flux to vary. The likelihood analysis was performed for the Part 1 and Part 2 light curves separately, and the resulting light curves and their ratios are shown in Fig. 8. The folded light curves are similar in overall properties to the folded probability-weighted aperture pho-

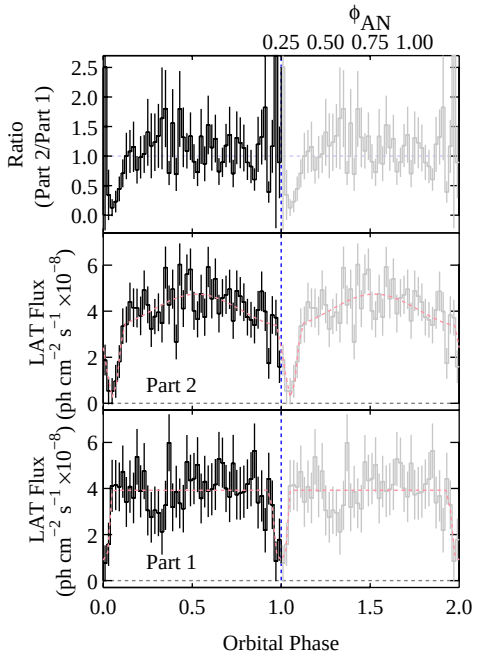

Figure 8. The binary phase-resolved flux of 4FGL J1702.7−5655 obtained from likelihood analysis of LAT observations. Spectral parameters were held fixed at the 4FGL catalog (DR2) values. Fits are shown for time ranges of MJD 54,682 - 56,345 (bottom) and 56,345 - 59,445 (middle). The top panel shows the ratio of the fluxes in the second part to the first part. The dashed pink lines in the bottom two panels indicate the fits made to the folded light curves, the parameters are given in Table 4. For clarity, for all panels two identical cycles are plotted with the second cycle plotted in gray. The vertical dashed blue lines show the eclipse center as determined for Part 1. The bottom X-axis uses eclipse center to define orbital phase zero. The upper labels show the predicted orbital phases with time of ascending node defining zero.

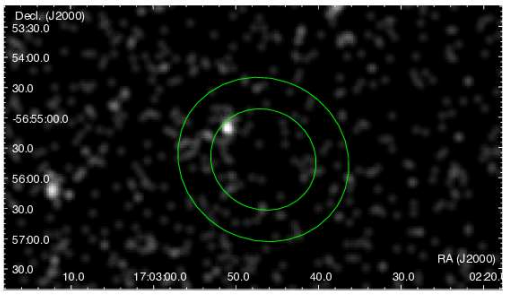

Figure 9. Smoothed Swift XRT image of the region around 4FGL J1702.7−5655. LAT 68 and 95% confidence regions are marked. The candidate X-ray counterpart is the brightest source within the 68% region.

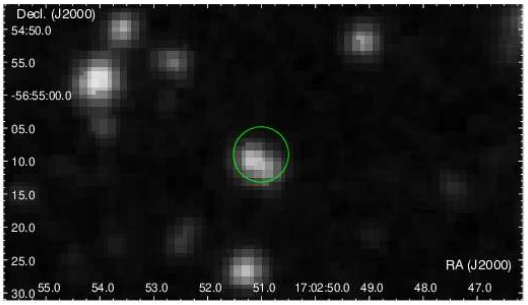

Figure 10. DSS2 red image of the region around the possible XRT counterpart of 4FGL J1702.7−5655. The XRT error region is marked.

tometry light curves (Fig. 2). However, it can now be seen that the minima during the eclipses are very close to zero flux, and given uncertainties in the background, are consistent with zero. To characterize these phase-resolved likelihood light curves we again fitted the same functions that we employed for the aperture photometry light curves. i.e. an eclipse profile for Part 1, and an eclipse profile plus sine component for Part 2. We kept the eclipse time parameters (center time, phase duration, phase of eclipse ingress and egress) held fixed at the values determined from fitting the aperture photometry light curves and only allowed the fluxes and the phase of the sine wave to be free. The results are given in Table 4 and overplotted on the light curves in Fig. 2. In this parameterization, the out-of-eclipse fluxes are consistent with being the same for both Part 1 and Part 2. The maximum of the sine wave component is again found to be 0.5 in phase away from the eclipse, i.e. at inferior conjunction. The sine wave semi-amplitude is 17 ± 4% of the out-of-eclipse flux. We note that the difference between the mean out-of-eclipse flux and the flux at eclipse minimum of (3.1 ± 0.5) $\times 10^{-8}$ ph cm^{-2} s^{-1} significantly exceeds the sine wave semi-amplitude of (0.70 ± 0.18) $\times 10^{-8}$ ph cm^{-2} s^{-1}.

3.2. *X-ray Results*

A smoothed image obtained from the Swift XRT observations is shown in Fig. 9. We find that there is an excess within the Fermi 68% error ellipse at $17^h02^m51^s.01, -56°55'09''.1$ with an uncertainty of $4.2''$. The detection signal-to-noise ratio is 3.7 with 34 counts compared to an expected background of 10. Due to the small number of counts it is not possible to obtain a spectrum of this candidate source. Of the total ∼17.5 ks XRT exposure time, only ∼3 ks was obtained during Part 1 of the light curve which also hampers an investigation of any change in X-ray flux associated with the change in the gamma-ray orbital modulation. In Fig. 10 we show the Deep Sky Survey 2 red image centered on the XRT location. Within the error region are several stars which are blended in this image. Optical spectroscopy of these stars is in process and will be published later (Swihart et al. in preparation).

3.3. *Radio Results*

Although several radio sources were detected within the ATCA field of view, none lie within the LAT error region. Hence, we are only able to obtain upper limits on the presence of a radio counterpart. From the summed images at each frequency we obtain 3σ upper limits at the source location of 66, 69, and 69 μJy at 2100, 5500 and 9500 MHz respectively. We note that in the second Fermi LAT catalog of gamma-ray pulsars ("2PC" Abdo et al. 2013), sources with flux densities $< 30\,\mu$Jy at 1400 MHz are regarded as radio quiet, and that most pulsars have spectral indices of -1.7. Thus, at $\sim$2000 MHz radio quiet sources would have flux densities $\lesssim 60\,\mu$Jy, which is comparable to our upper limits and hence we cannot yet exclude the presence of a radio pulsar.

4. DISCUSSION

4.1. *The Characteristics of the Orbital Modulation in 4FGL J1702.7−5655*

The sharp dip seen in both the earlier and later portions of the light curve is consistent with an eclipse of the gamma-ray emitting region by a companion star in a highly inclined orbit. This is thus consistent with the proposed classification as a redback system. The presence of strong modulation seen in the power spectrum of the LAT light curve is exceptional for binary MSPs. The detection of the period is related to the change in orbital modulation. When tMSPs undergo state changes, larger flux variations are seen (e.g. Roy et al. 2015) than the somewhat modest change in orbital profile seen for 4FGL J1702.7−5655 which is not accompanied by large changes in the gamma-ray flux or spectrum.

We next review orbital modulation in other binary MSPs as previously reported from LAT observations for comparison with 4FGL J1702.7−5655. For several systems we also consider the properties of this modulation as found from our program. The parameters of these systems are summarized in Table 5. For 4FGL J1702.7−5655 we have used the center of the eclipse to define orbital phase 0. For most systems discussed here pulse timing orbits have been derived, but no eclipses have been observed. Hence for these systems typically the time of the ascending node is used to define orbital phase (ϕ_{AN}) 0. For a circular orbit where the gamma-ray emission is centered on the neutron star, the ascending node will occur 0.25 in phase earlier than an eclipse. i.e. an eclipse would be expected to occur at superior conjunction of the pulsar at $\phi_{AN} = 0.25$, and inferior conjunction of the pulsar (compact object nearest us) would occur at $\phi_{AN} = 0.75$.

4.2. *Comparison with Orbital Modulation of Gamma-ray Emission in Other Systems*

4.2.1. *Other Eclipsing MSP Systems*

To investigate whether any of the other known gamma-ray eclipsing MSP systems (Strader et al. 2016; Kennedy et al. 2020; Clark et al. 2021b) also show any quasi-sinusoidal modulation, which could be a sign that such modulation depends on the inclination angle of a system, we calculated the power spectra of the LAT light curves of these sources around their orbital periods and these are plotted in Fig. 11. For no other eclipsing system is the orbital period detectable in the power spectrum, although we note that these systems are all fainter than

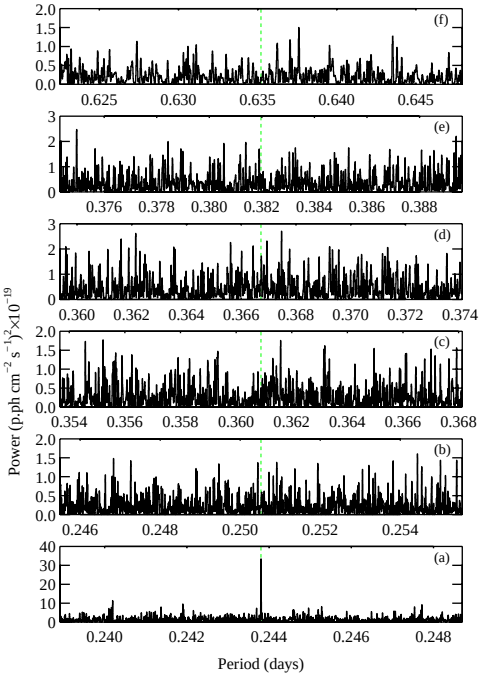

Figure 11. A comparison of the power spectrum of 4FGL J1702.7−5655 with the power spectra of probability-weighted aperture photometry for likely redback systems for which eclipses have been reported and are present in the 4FGL DR2 catalog. Power spectra are centered on the orbital periods (Table 5), which are marked by the vertical dashed green line. (a) 4FGL J1702.7−5655, (b) 4FGL J1048.6+2340 (PSR J1048+2339), (c) 4FGL J1816.5+4510 (PSR J1816+4510), (d) 4FGL J0427.8−6704, (e) 4FGL J1959.5+2048 (PSR B1957+20), (f) 4FGL J2129.8−0428 (PSR J2129−0429).

4FGL J1702.7−5655 (Table 5). For PSR B1957+20, we note that Wu et al. (2012) reported orbital modulation of > 2.7 GeV gamma rays from Fermi LAT observations with a maximum near the phase of radio eclipse, i.e. pulsar superior conjunction at ϕ_{AN} $\sim$0.25. We also calculated a probability weighted aperture photometry light curve for 4FGL J1959.5+2048 (PSR B1957+20) for energies above 2.7 GeV. However, the power spectrum of this does not show any modulation at the orbital period, and folding the light curve on the orbital period also did not reveal orbital modulation.

4.2.2. *4FGL J2039.5-5617 (PSR J2039−5617)*

The redback system 4FGL J2039.5-5617 (= PSR J2039−5617, 3FGL 2039.6-5618, "J2039.5") was found to have its gamma-ray emission as measured with the LAT modulated on its 0.228 day orbital period with an approximately sinusoidal profile by Ng et al. (2018). The phasing of the gamma-ray modulation in J2039.5 is that it has a maximum at $\phi_{AN} = 0.25 \pm 0.03$ (Clark et al. 2021a), i.e. superior conjunction. The maximum of the sinusoidal modulation in 4FGL J1702.7−5655 is thus 0.5 out of phase with that in J2039.5, if the eclipse is indeed that of the compact object in the system. Ng et al. (2018) suggested that the amplitude of the orbital modulation had decreased after $\sim$MJD 57,000. Such a change in the sinusoidal modulation could indicate a similarity with 4FGL J1702.7−5655. Clark et al. (2021a) subsequently detected gamma-ray pulsations using the LAT at a period of 2.65 ms. However, Clark et al. (2021a) found that

the orbital modulation increased again after MJD 58,100 and suggested that this could be due to statistical variations rather than intrinsic changes in the source. Ng et al. (2018) and Clark et al. (2021a) noted that the time of apparent decrease in orbital modulation coincided with an outburst from the blazar candidate 4FGL J2052.2−5533 (3FGL J2051.8–5535) which lies only 1.9° from J2039.5 and experienced a flare around ∼56,500 to 57,500.

Our power spectrum of the LAT light curve of J2039.5 is shown in Fig. 12. In the bottom panel, which covers the entire frequency range, the strongest peak is near 1 day, and this is a commonly seen artifact in the power spectra of LAT light curves. The second strongest peak is at a period of 2429 ± 112 days and this long-period/low-frequency peak may be due to contamination from 4FGL J2052.2−5533. The third strongest peak is at the orbital period of J2039.5. The frequency range around this is plotted in the upper panel of Fig. 12. The period we derive is 0.227978(1), consistent at a 1.8σ level with the period of 0.227979805(3) days found by Clark et al. (2021a) from pulse timing. The relative height of the peak is 17 which corresponds to an FAP of 0.004 (i.e. 99.6% significance) for a blind search over the entire frequency range, and 4×10^{-8} for a single-frequency trial. We note the presence of a peak almost as strong as the orbital modulation close to the orbital period at 0.225601(1) days. While Clark et al. (2021a) reported variations in the orbital period of J2039.5, these have a total range of $\Delta P/P$ $\sim10^{-6}$ and so would not result in the second peak with a period difference of ∼1%. We speculate that this peak is caused by aliasing, although it would be unclear how this is arising as the frequency difference between these nearby peaks corresponds to a period of ∼21.6 days. We note that J2039.5 is rather fainter than 4FGL J1702.7−5655 which can account for the lower relative height of the modulation in J2039.5 even if both sources had similar variability.

We next investigated the rate of change of the orbital peak in the power spectrum as a function of light curve length in a similar way to our analysis of 4FGL J1702.7−5655. Consistent with Ng et al. (2018) and Clark et al. (2021a), we find a decrease in the rate of relative peak height change with light curve length between approximately MJD 57,000 to 58,000. But we again cannot necessarily attribute this to a reduction in modulation strength as this coincides with the flare in 4FGL J2052.2−5533. To investigate further we calculated power spectra for 1000 day long time intervals and these are show in Fig. 13. We find that for segment (c), which covers MJD 57,000 to 58,000, modulation is not seen at the orbital period, although there is not a large change in the continuum power level. This may suggest that during this time the lack of detection of orbital modulation may be because of reduced amplitude, and not just because of an increase in the background noise level due to the AGN flare. Nevertheless, the temporal coincidence with this flare does hinder a unambiguous determination that there was indeed a reduction in orbital gamma-ray modulation.

4.2.3. *Quasi-Sinusoidal Modulation of Pulsed Emission in 4FGL J2339.6−0533 (PSR J2339−0533)*

The redback PSR J2339−0533 (4FGL J2339.6−0533, "J2239.6") shows quasi-sinusoidal modulation of the

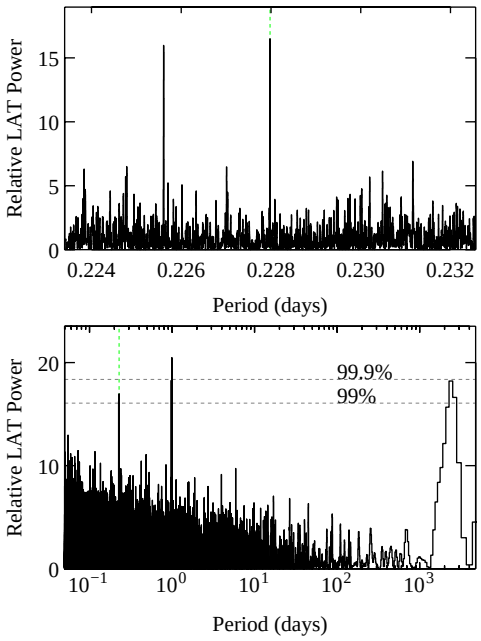

Figure 12. Power spectra of the probability-weighted aperture photometry LAT light curve of 4FGL J2039.5−5617 (= PSR J2039−5617). The bottom panel shows a range from 0.05 days to the length of the light curve, while the top panel shows the detail around the orbital period of 4FGL J2039.5−5617 which is marked with dashed green lines in both panels. The peak near one day in the bottom panel is a common artifact seen in the power spectra of many LAT sources.

LAT flux on the ∼0.193 day orbital period (An et al. 2020). However, in this system it is the *pulsed* gamma-ray emission of the 2.9 ms pulsar that is orbitally modulated which is difficult to explain. For J2239.6 the orbital maximum occurs near superior conjunction (when the neutron star is farthest from us) which is similar to J2039.5, but again apparently 0.5 out of phase with 4FGL J1702.7−5655. In J2239.6, similar to other binary MSPs where orbital modulation has been claimed, the gamma-ray modulation was not found from a blind search but relied on the orbital period already being known. For J2339.6 we do not detect significant modulation from our probability-weighted aperture photometry light curve, consistent with the report by An et al. (2020) that orbital modulation is only present in the on-pulse.

4.2.4. *The Transitional Source XSS J12270−4859 (4FGL J1228.0−4853)*

XSS J12270−4859 (4FGL J1228.0−4853, PSR J1227−4853) is a transitioning redback that switched from an LMXB to an MSP state in 2012 (Bassa et al. 2014). An (2022) reported that the gamma-ray flux (60 MeV - 1GeV) was modulated on the ∼0.29 day orbital period of the system, with *minimum* at inferior conjunction of the orbit (ϕ_{AN}=0.75), and maximum near superior conjunction (ϕ_{AN}=0.25). Curiously, An (2022) found that the orbital gamma-ray modulation was similar in both the MSP and LMXB states. However, Xing & Wang (2015) had previously reported the presence of orbital modulation in LAT gamma-ray observations (> 200 MeV) with a *maximum* near inferior

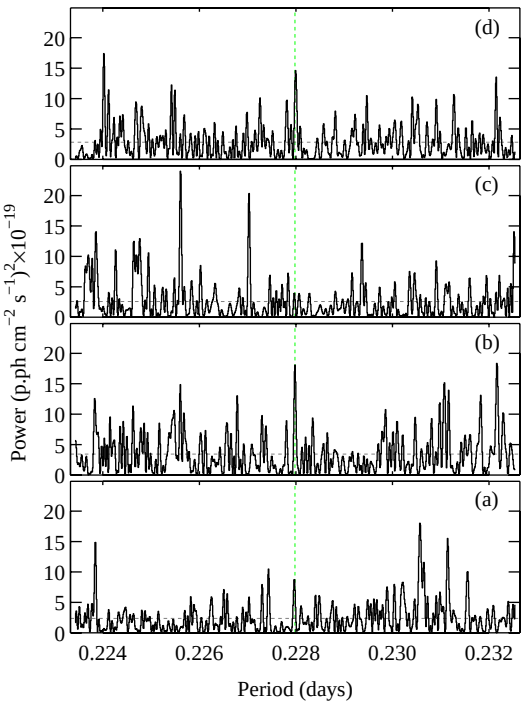

Figure 13. Power spectra of the probability-weighted aperture photometry LAT light curve of 4FGL J2039.5−5617 (= PSR J2039−5617) divided into time segments: (a) MJD 55000 - 56000, (b) MJD 56,000 - 57,000, (c) MJD 57,000 - 58,000, (d) MJD 58,000 - 59,000. The orbital period of 4FGL J2039.5−5617 is marked with dashed vertical green lines in all panels, and the dashed horizontal gray lines show the mean power levels

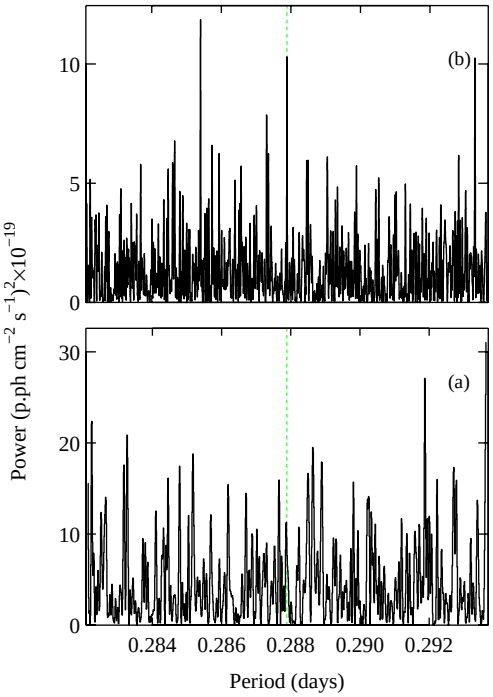

Figure 14. Power spectra of the probability-weighted aperture photometry LAT light curves of the transitional MSP XSS J12270−4859 (4FGL J1228.0−4853) for the time intervals of (a) MJD 54,682 - 56,250 and (b) MJD 56,250 - 59,445. The orbital period (Table 5) is marked by the dashed green lines.

conjunction (ϕ_{AN}=0.75) that was only seen after the transition to the MSP state.

To investigate the presence of orbital modulation in our 100 MeV - 500 GeV light curve of 4FGL J1228.0−4853 we calculated power spectra for the time intervals before and after MJD 56,250 (2012 November 19), and these are shown in Fig. 14. For the earlier time interval when XSS J12270−4859 was in an LMXB state we do not detect orbital modulation. However, for the later time interval when the source had transitioned to an MSP state,we see a peak at a period of 0.287888(3), consistent with the orbital period. The peak's relative height is 7.8, which corresponds to a single trial FAP of 4×10^{-4}. The detection of orbital modulation only in the MSP state is similar to the result of Xing & Wang (2015). However, the light curves for the same time intervals folded on the orbital period (Fig. 15) show that for the later time interval the highest flux is at ϕ_{AN}∼0.25, similar to the result of An (2022).

4.2.5. *The Black Widows PSR J1311−3430 and PSR J2241−5236*

Orbital modulation in the *off*-pulse emission has also been reported for the black widow systems PSR J1311−3430 (4FGL J1311.7−3430, "J1311.7"; Xing & Wang 2015; An et al. 2017) and PSR J2241−5236 (4FGL J2241.7−5236, "J2241.7"; An et al. 2018). For J1311.7 the maximum occurs at $\phi_{AN} = 0.8$, i.e. near inferior conjunction and minimum at $\phi_{AN} = 0.4$. For J2241.7 maximum occurs at superior conjunction (ϕ_{AN} 0.25) with a possible secondary maximum at $\phi_{AN} = 0.75$.

While these systems did not appear in our blind

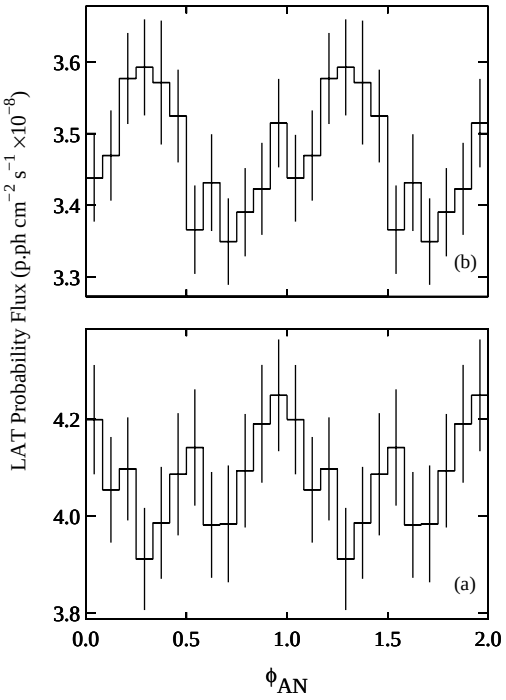

Figure 15. Probability-weighted aperture photometry LAT light curves of the transitional MSP XSS J12270−4859 (4FGL J1228.0−4853) folded on the orbital period for the time ranges of (a) MJD 54,682 - 56,250 and (b) MJD 56,250 - 59,445. Phase zero was defined as 56700.9070772, corresponding to "Solution 1" from An (2022).

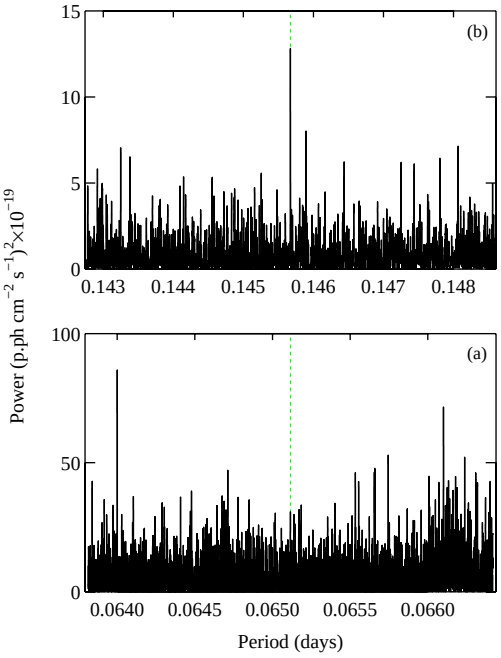

Figure 16. Power spectra of the probability-weighted aperture photometry LAT light curves of the black widow systems 4FGL J1311.7−3430 (bottom) and 4FGL J2241.7−5236 (top). The orbital periods (Table 5) are marked by the dashed green lines.

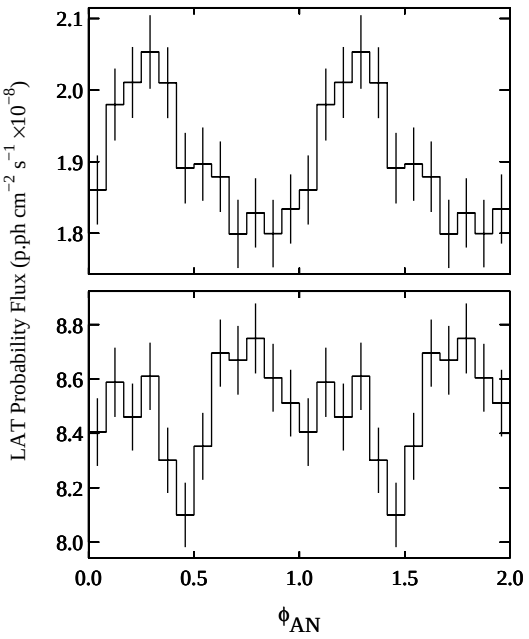

Figure 17. The probability-weighted aperture photometry LAT light curves of the black widow systems 4FGL J1311.7−3430 (bottom) and 4FGL J2241.7−5236 (top) folded on their orbital periods (Table 5).

search for periodicities, power spectra centered around the known periods do show an indication of modulation for J2241.7 (Fig. 16). In the full frequency range blind search this period is not readily detectable as its relative height is only ∼13 (FAP = 0.19), and it is the second highest peak after the 1-day artifact. However, for a single trial the FAP is $\sim 2\times10^{-6}$. No power spectrum peak is seen for J1311.7 (Fig. 16) - for this source we also investigated using shorter time bins of 100 s due to the short (0.065 day) orbital period and no change to the power spectrum was found. Folding the aperture photometry light curves on the known periods (Fig. 17) does show modulation for both systems. The modulation is thus detectable in the overall emission from both systems without pulse phase selection. For both sources we see orbital maximum at the same phases as previously reported (An et al. 2017, 2018). There thus appears not to be any large difference in the pulse-averaged profiles with the orbital profiles seen in the off-pulse emission, although the amplitudes are lower.

4.3. *Implications for 4FGL J1702.7−5655*

The gamma-ray variability in 4FGL J1702.7−5655 is characterized by two modes of periodic behavior. In Part 1 of the light curve the only modulation clearly present is the rather sharp dip that reduces to a level consistent with the background. Then, this transitions to a combination of a dip in the light curve at a slightly later phase together with the appearance of quasi-sinusoidal modulation. This change in periodic behavior is not accompanied by a significant change in the overall gamma-ray brightness or spectral parameters. While some aspects of the variability of 4FGL J1702.7−5655 have been seen before in other sources, this combination of eclipses, and transient (on timescales of years) quasi-sinusoidal modulation has not previously been reported.

The light curve dip in Part 2 reaches a similarly low level to that during Part 1, which implies that the gamma-ray emitting region is still sufficiently small to be totally eclipsed. However, the minimum occurs later by ∼0.05 in phase. i.e. the gamma-ray emission region is trailing the previous center of emission by ∼15°. In addition, the gamma-ray emission now has a non-isotropic component which results in quasi-sinusoidal orbital modulation with a semi-amplitude of 17 ± 4%. Since pulsations have not yet been detected from 4FGL J1702.7−5655, we cannot determine whether the orbital modulation in Part 2 is pulse-phase dependent.

The X-ray brightness of 4FGL J1702.7−5655 is low, which suggests that the system has not transitioned to an accreting LMXB state. While we do not yet have an accurate measurement of the X-ray spectrum, or a distance to the source, we can make a rough estimate of the X-ray to gamma-ray flux (F_X/F_γ). At a count rate of $\sim 1.4\times10^{-3}\,\mathrm{cts\,s^{-1}}$, we adopt a power-law spectrum with a photon-index of 1.75 and $N_H = 1.25\times10^{21}\,\mathrm{cm^{-2}}$ (HI4PI Collaboration et al. 2016), using PIMMS[14] the unabsorbed 0.5 - 10 keV flux is $6\times10^{-14}\,\mathrm{erg\,cm^{-2}\,s^{-1}}$. The ratio F_X/F_γ, using the LAT catalog 0.1 - 100 GeV flux (Table 5), is 0.002. Although this has considerable uncertainty, it is much lower than the values of ∼0.25 - 0.4 for tMSPs in the sub-luminous disk state reported by Miller et al. (2020). If the XRT source is not the counterpart of 4FGL J1702.7−5655, then the ratio of

[14] https://heasarc.gsfc.nasa.gov/cgi-bin/Tools/w3pimms/w3pimms.pl

F_X/F_γ must be even lower. Nevertheless, even though 4FGL J1702.7−5655 apparently did not transition to an LMXB state, some type of change did occur to the system.

Although we do not yet have a Doppler orbit for 4FGL J1702.7−5655, it appears highly likely that the "eclipse" is indeed the superior conjunction of a pulsar (non-degenerate object nearest us). The short ingress and egress, and the minimum being consistent with zero flux, indicate an eclipse rather than a change in absorption or emission due to the changing system geometry. Were it not an eclipse, the inclination would have to be smaller than about 80° given the orbital period and typical masses of such systems. The angle dependencies of inverse Compton scattering, absorption due to pair production or Doppler boosted emission would then produce a smoother modulation and would be unlikely to produce zero flux. Given the greater penetrating power of gamma-rays compared to X-rays or radio waves, a much more substantial amount of material is required to cause significant absorption. Due to this, while radio and X-ray emission can be attenuated by, for example, winds, to cause a ∼100% drop in gamma-rays requires the body of a star (e.g. Clark et al. 2021b).

For Part 1 of the light curve, where the orbital modulation is apparently less complicated, the total eclipse duration (ingress start to egress end) is 0.110 ± 0.038 in phase, corresponding to a half-angle of $19.8 \pm 6.8°$. For comparison, the X-ray eclipse in 4FGL J0427.8−6704 has a half-angle of $12.5 \pm 0.3°$ (Strader et al. 2016). Chanan et al. (1976) derived eclipse durations for point sources with Roche-lobe filling companions, although these are degenerate between inclination angle and mass ratio, q (mass of Roche-lobe filling star/mass of point source). For an inclination angle of 90°, $q \gtrsim 0.25$. Similarly, applying the transit equation of Seager & Mallén-Ornelas (2003) implies a companion mass $> 0.85\ M_\odot$ to avoid it overfilling its Roche lobe. If, similar to Strader et al. (2016), we consider the possibility that the system could have an inclination of as low as 75°, the eclipse duration then requires $q \gtrsim 1$, although that would imply a surprisingly massive companion star. Strader et al. (2019) find a mean mass for redback companions of 0.36 ± 0.04 $M_\odot$ with a σ of $0.15 \pm 0.04\ M_\odot$, while black widow companions have companions $< 0.05\ M_\odot$. If the gamma-ray source is extended, then the constraints on the companion mass are less stringent, however the sharpness of the ingress and egress (∼0.02 in phase) limits the extension of the gamma-ray source to less than $\sim 0.2\ R_\odot$ which sets a lower limit on the companion mass of $0.2\ M_\odot$. The companion is very unlikely to be less massive, as this would imply a gamma-ray emission size larger than the size of the star, producing a non-zero residual flux during the eclipse and a slower ingress and egress. We conclude that the companion for 4FGL J1702.7−5655 is more likely to be similar to those of redback systems than the very low mass companions of black widow systems and that, particularly for Part 1, the gamma-ray emission is not highly extended.

For the spider systems with orbital modulation of gamma-ray flux (excluding eclipses by the secondary) there is as yet no definite explanation for this. In addition, there is a difference in systems where the modulation is primarily in the pulsed or non-pulsed emission. For 4FGL J2039.5-5617, Ng et al. (2018) suggested that the orbital modulation may be due to Compton scattering of soft photons from the companion and the relativistic pulsar wind. For 4FGL J2339.6−0533, where the *pulsed* emission is modulated, An et al. (2020) discuss several scenarios, also including Compton scattering from the companion. In 4FGL J1311.7−3430 for the *off*-pulse orbital modulation at energies > 200 MeV An et al. (2017) discuss bulk plasma motion in the IBS. For systems where quasi-sinusoidal orbital modulation of gamma-ray emission has been reported, this is generally seen to peak near superior conjunction (Table 5), unlike what is expected to be the case for 4FGL J1702.7−5655. 4FGL J1311.7−3430 does show a peak near inferior conjunction. It also exhibits a secondary peak near superior conjunction. Such a secondary peak would be more difficult to detect in 4FGL J1702.7−5655 due to the eclipse.

If 4FGL J1702.7−5655 has not changed between pulsar and accretion regimes, this indicates that some other change has occurred. For the Part 1 light curve where the only orbital modulation is the relatively sharp eclipse, we speculate that we are seeing magnetospheric emission from a pulsar in the system that is not strongly affected by other components in the system. Then during the latter portion of the light curve (i.e. Part 2) some other change occurred in the system. Modulation of the gamma-rays by Compton scattering off the companion star would produce a peak at superior conjunction. However, modulation due to Doppler boosting of the emission produced in the IBS would produce a maximum at inferior conjunction if the pulsar wind is collimated away from the star, wrapping around the pulsar as generally observed in redback systems (e.g. An et al. 2020). The change in the modulated lightcurve would then be due to variability in the IBS emission region. The formation and structure of an IBS in a binary MSP depends on the pressure balances due to winds from the binary components and the pulsar magnetosphere, however the roles of these are still incompletely understood (see e.g. Wadiasingh et al. 2017, 2018; van der Merwe et al. 2020). At least qualitatively, a change in the relative contributions to the gamma-ray emission from a pulsar and an IBS could explain the observed behavior, including the shift in the timing of the eclipse and its duration since the IBS emission is not necessarily centered on the pulsar and has a large spatial extent. However, it is challenging to determine why a change to the IBS occurred, why this should be ∼stable on timescales of years, and why the flux is not substantially changed due to this transition.

There is, however, some observational evidence that changes to the IBS in binary MSPs may occur. Polzin et al. (2020) reported that in low-frequency radio observations of eclipses in the redback system PSR J1816+4510 they found that the radio eclipse mechanism transitioned between one where pulsar emission was removed from the line of sight to one where the pulsations were smeared out. These authors attributed this to a tail of material trailing the pulsar's companion. In the redback 47 Tuc W, Hebbar et al. (2021) found that Chandra observations showed that orbital modulation of X-rays was not always present. They suggested that this was due to changes in the system's IBS. For XSS J12270-4859 (4FGL J1228.0−4853) de Martino et al. (2020) found that the orbital X-ray light curve orbital modu-

lation amplitude varied on timescales of a few months that could be due to a non-stationary contribution of the IBS. In addition, optical observations of the redback PSR J1048+2339 (4FGL J1048.6+2340) suggest changes to the IBS on timescales as short as two weeks (Yap et al. 2019). We speculate that the changes in the orbital gamma-ray modulation of 4FGL J1702.7−5655 might be due to similar changes to an IBS to those that occurred in these systems. In 4FGL J1702.7−5655 we have the advantage of the eclipses which may serve as a way of more precisely determining emission sites. If there is a change in the IBS in 4FGL J1702.7−5655, then measurements of the X-ray orbital variability, and particularly any changes in this associated with a gamma-ray state change, may be a crucial diagnostic.

5. CONCLUSION

The gamma-ray modulation found in 4FGL J1702.7−5655 is exceptional with its combination of both an eclipse and a quasi-sinusoidal component. The sinusoidal component also has a maximum near inferior conjunction which is exceptional. The change in the orbital profile also appears to be unprecedented, which indicates some change in state, although it is not accompanied by a large change in the gamma-ray flux or spectrum. To better understand the nature of this source, determining the optical counterpart and its properties and long-term multiwavelength monitoring are important to determine what changes occur during the state change and how this may connect to "traditional" tMSPs. Searches for millisecond pulsations in 4FGL J1702.7−5655 are important, and the determination of Doppler orbits from both pulse timing and optical radial velocity studies are necessary for determining system parameters, and thus understanding the nature of this system. Together with the eclipses, which measure the location of emissions region in the system, these may provide the keys to unlock the physics at work in this system. Continued monitoring of other sources in the Fermi-LAT catalogs has the potential to detect a similar system if the same type of change in its orbital modulation occurs, or the accumulation of additional data enables the detection of existing modulation. 4FGL J2039.5−5617 should also continue to be monitored to determine whether its quasi-sinusoidal modulation does indeed also change on similar timescales to that in 4FGL J1702.7−5655.

We thank Matthew Kerr and Zorawar Wadiasingh for useful comments. This work was partially supported by NASA Fermi grant 80NSSC21K2029 and also under NASA award number 80GSFC21M0002. J. Strader acknowledges support from a Packard Fellowship. This work was partially supported by NASA grant 80NSSC17K0507 and NSF grant AST-1714825. Portions of this work was performed while SJS held a NRC Research Associateship award at the Naval Research Laboratory. Work at the Naval Research Laboratory is supported by NASA DPR S-15633-Y. The Australia Telescope Compact Array is part of the Australia Telescope National Facility which is funded by the Australian Government for operation as a National Facility managed by CSIRO who acknowledge the Gomeroi people as the traditional owners of the Observatory site. We thank the Swift team for undertaking observations and this work made use of data supplied by the UK Swift Science Data Centre at the University of Leicester. The *Fermi* LAT Collaboration acknowledges generous ongoing support from a number of agencies and institutes that have supported both the development and the operation of the LAT as well as scientific data analysis. These include the National Aeronautics and Space Administration and the Department of Energy in the United States, the Commissariat à l'Energie Atomique and the Centre National de la Recherche Scientifique / Institut National de Physique Nucléaire et de Physique des Particules in France, the Agenzia Spaziale Italiana and the Istituto Nazionale di Fisica Nucleare in Italy, the Ministry of Education, Culture, Sports, Science and Technology (MEXT), High Energy Accelerator Research Organization (KEK) and Japan Aerospace Exploration Agency (JAXA) in Japan, and the K. A. Wallenberg Foundation, the Swedish Research Council and the Swedish National Space Board in Sweden. Additional support for science analysis during the operations phase is gratefully acknowledged from the Istituto Nazionale di Astrofisica in Italy and the Centre National d'Études Spatiales in France.

REFERENCES

Abdo, A. A., Ackermann, M., Ajello, M., et al. 2010, ApJS, 188, 405
Abdo, A. A., Ajello, M., Allafort, A., et al. 2013, ApJS, 208, 17. doi:10.1088/0067-0049/208/2/17
Abdollahi, S., Acero, F., Ackermann, M., et al. 2020, ApJS, 247, 33. doi:10.3847/1538-4365/ab6bcb
Acero, F., Ackermann, M., Ajello, M., et al. 2015, ApJS, 218, 23
Ajello, M., Atwood, W. B., Axelsson, M., et al. 2021, ApJS, 256, 12. doi:10.3847/1538-4365/ac0ceb
An, H., Romani, R. W., Johnson, T., et al. 2017, ApJ, 850, 100. doi:10.3847/1538-4357/aa947f
An, H., Romani, R. W., & Kerr, M. 2018, ApJ, 868, L8. doi:10.3847/2041-8213/aaedaf
An, H., Romani, R. W., Kerr, M., et al. 2020, ApJ, 897, 52. doi:10.3847/1538-4357/ab93ba
An, H. 2022, ApJ, 924, 91. doi:10.3847/1538-4357/ac36ca
Arzoumanian, Z., Fruchter, A. S., & Taylor, J. H. 1994, ApJ, 426, L85. doi:10.1086/187346
Atwood, W. B., Abdo, A. A., Ackermann, M., et al. 2009, ApJ, 697, 1071
Baluev, R. V. 2008, MNRAS, 385, 1279
Bassa, C. G., Patruno, A., Hessels, J. W. T., et al. 2014, MNRAS, 441, 1825. doi:10.1093/mnras/stu708
Breton, R. P., van Kerkwijk, M. H., Roberts, M. S. E., et al. 2013, ApJ, 769, 108. doi:10.1088/0004-637X/769/2/108
Bruel, P., Burnett, T. H., Digel, S. W., et al. 2018, arXiv:1810.11394
Bulgarelli, A., Fioretti, V., Parmiggiani, N., et al. 2019, A&A, 627, A13. doi:10.1051/0004-6361/201834143
Burrows, D. N., Hill, J. E., Nousek, J. A., et al. 2005, Space Sci. Rev., 120, 165
Camilo, F., Kerr, M., Ray, P. S., et al. 2015, ApJ, 810, 85. doi:10.1088/0004-637X/810/2/85
Chanan, G. A., Middleditch, J., & Nelson, J. E. 1976, ApJ, 208, 512. doi:10.1086/154633
Clark, C. J., Wu, J., Pletsch, H. J., et al. 2017, ApJ, 834, 106
Clark, C. J., Nieder, L., Voisin, G., et al. 2021a, MNRAS, 502, 915. doi:10.1093/mnras/staa3484
Clark, C. J., et al. 2021b, Ninth International Fermi Symposium, https://indico.cern.ch/event/1010947/contributions/4301985/attachments/22
Corbet, R. H. D., Chomiuk, L., Coe, M. J., et al. 2019, ApJ, 884, 93. doi:10.3847/1538-4357/ab3e32

de Martino, D., Papitto, A., Burgay, M., et al. 2020, MNRAS, 492, 5607. doi:10.1093/mnras/staa164
Deneva, J. S., Ray, P. S., Camilo, F., et al. 2016, ApJ, 823, 105. doi:10.3847/0004-637X/823/2/105
Evans, P. A., Beardmore, A. P., Page, K. L., et al. 2009, MNRAS, 397, 1177. doi:10.1111/j.1365-2966.2009.14913.x
Fermi LAT Collaboration, Ackermann, M., Ajello, M., et al. 2012, Science, 335, 189
Gentile, P. A., Roberts, M. S. E., McLaughlin, M. A., et al. 2014, ApJ, 783, 69. doi:10.1088/0004-637X/783/2/69
Goad, M. R., Tyler, L. G., Beardmore, A. P., et al. 2007, A&A, 476, 1401. doi:10.1051/0004-6361:20078436
Grießmeier, J.-M., Smith, D. A., Theureau, G., et al. 2021, A&A, 654, A43. doi:10.1051/0004-6361/202140841
HI4PI Collaboration, Ben Bekhti, N., Flöer, L., et al. 2016, A&A, 594, A116. doi:10.1051/0004-6361/201629178
Hebbar, P. R., Heinke, C. O., Kandel, D., et al. 2021, MNRAS, 500, 1139. doi:10.1093/mnras/staa3072
Horne, J. H., & Baliunas, S. L. 1986, ApJ, 302, 757
Kandel, D., Romani, R. W., & An, H. 2019, ApJ, 879, 73. doi:10.3847/1538-4357/ab24d9
Kennedy, M. R., Breton, R. P., Clark, C. J., et al. 2020, MNRAS, 494, 3912. doi:10.1093/mnras/staa912
Kerr, M. 2011, ApJ, 732, 38
Kerr, M. 2019, ApJ, 885, 92. doi:10.3847/1538-4357/ab459f
Kong, A. K. H., Takata, J., Hui, C. Y., et al. 2018, MNRAS, 478, 3987. doi:10.1093/mnras/sty1459
Lampton, M., Margon, B., & Bowyer, S. 1976, ApJ, 208, 177. doi:10.1086/154592
Levine, A. M., Bradt, H. V., Chakrabarty, D., et al. 2011, ApJS, 196, 6. doi:10.1088/0067-0049/196/1/6
Miller, J. M., Swihart, S. J., Strader, J., et al. 2020, ApJ, 904, 49. doi:10.3847/1538-4357/abbb2e
Ng, C. W., Takata, J., Strader, J., et al. 2018, ApJ, 867, 90. doi:10.3847/1538-4357/aae308
Nolan, P. L., Abdo, A. A., Ackermann, M., et al. 2012, ApJS, 199, 31
Papitto, A. & de Martino, D. 2020, arXiv:2010.09060
Polzin, E. J., Breton, R. P., Bhattacharyya, B., et al. 2020, MNRAS, 494, 2948. doi:10.1093/mnras/staa596
Roberts, M. S. E. 2013, Neutron Stars and Pulsars: Challenges and Opportunities after 80 years, 291, 127. doi:10.1017/S174392131202337X
Roberts, M. S. E., Mclaughlin, M. A., Gentile, P., et al. 2014, Astronomische Nachrichten, 335, 313. doi:10.1002/asna.201312038
Romani, R. W. & Shaw, M. S. 2011, ApJ, 743, L26. doi:10.1088/2041-8205/743/2/L26
Roy, J., Ray, P. S., Bhattacharyya, B., et al. 2015, ApJ, 800, L12. doi:10.1088/2041-8205/800/1/L12
Seager, S. & Mallén-Ornelas, G. 2003, ApJ, 585, 1038. doi:10.1086/346105
Sault, R. J., Teuben, P. J., & Wright, M. C. H. 1995, Astronomical Data Analysis Software and Systems IV, 77, 433
Saz Parkinson, P. M., Xu, H., Yu, P. L. H., et al. 2016, ApJ, 820, 8
Scargle, J. D. 1982, ApJ, 263, 835
Stovall, K., Lynch, R. S., Ransom, S. M., et al. 2014, ApJ, 791, 67. doi:10.1088/0004-637X/791/1/67
Strader, J., Li, K.-L., Chomiuk, L., et al. 2016, ApJ, 831, 89. doi:10.3847/0004-637X/831/1/89
Strader, J., Swihart, S., Chomiuk, L., et al. 2019, ApJ, 872, 42. doi:10.3847/1538-4357/aafbaa
Stroh, M. C. & Falcone, A. D. 2013, ApJS, 207, 28. doi:10.1088/0067-0049/207/2/28
van der Merwe, C. J. T., Wadiasingh, Z., Venter, C., et al. 2020, ApJ, 904, 91. doi:10.3847/1538-4357/abbdfb
VanderPlas, J. T. 2018, ApJS, 236, 16
Vaughan, S. 2005, A&A, 431, 391. doi:10.1051/0004-6361:20041453
Wadiasingh, Z., Harding, A. K., Venter, C., et al. 2017, ApJ, 839, 80. doi:10.3847/1538-4357/aa69bf
Wadiasingh, Z., Venter, C., Harding, A. K., et al. 2018, ApJ, 869, 120. doi:10.3847/1538-4357/aaed43
Wilson, W. E., Ferris, R. H., Axtens, P., et al. 2011, MNRAS, 416, 832
Wu, E. M. H., Takata, J., Cheng, K. S., et al. 2012, ApJ, 761, 181. doi:10.1088/0004-637X/761/2/181
Wu, J., Clark, C. J., Pletsch, H. J., et al. 2018, ApJ, 854, 99
Xing, Y. & Wang, Z. 2015, ApJ, 804, L33. doi:10.1088/2041-8205/804/2/L33
Xing, Y. & Wang, Z. 2015, ApJ, 808, 17. doi:10.1088/0004-637X/808/1/17
Yap, Y. X., Li, K. L., Kong, A. K. H., et al. 2019, A&A, 621, L9. doi:10.1051/0004-6361/201834545
Zechmeister, M. & Kürster, M. 2009, A&A, 496, 577. doi:10.1051/0004-6361:200811296

Table 1
Swift XRT Observations of 4FGL J1702.7−5655

Observation Start (UT Date)	Observation End (UT Date)	Exposure (s)
2011-11-01 19:58	2011-11-01 21:50	1220
2012-06-26 05:06	2012-06-26 05:12	280
2012-10-30 21:20	2012-10-30 21:36	810
2012-11-06 19:54	2012-11-06 20:16	915
2016-11-04 11:51	2016-11-04 19:55	1935
2021-02-06 02:13	2021-02-06 23:20	4435
2021-02-15 01:51	2021-02-16 22:28	1145
2021-03-03 00:00	2021-03-03 05:01	1385
2021-03-04 03:11	2021-03-04 22:28	5535

Note. — The line indicates the division between Part 1 and Part 2 of the LAT light curve (MJD 56,345 = 2013-02-22).

Table 2
Australia Telescope Compact Array Radio Observations of
4FGL J1702.7−5655

Observation Start (UT Date)	MJD	Configuration	Center Frequency (MHz)	Duration (minutes)
2020 Dec 25	59208	1.5A	2100	541.1
2021 Jan 07	59221	1.5A	2100	759.3
2021 Jan 14	59228	EW352	2100	308.7
2021 Jan 16	59230	EW352	2100	778.6
2021 Nov 22	59540	6C	5500/9000	68.9

Note. — The first four observations used $17^h02^m46^s.68, -56°55'41''.88$ as the target position, while the last used $17^h02^m51^s.45, -56°55'09''.69$. The ATCA array configurations are the standard names for the physical locations of the antennas: see https://www.narrabri.atnf.csiro.au/operations/array_configurations/configurations.html for full details of the antenna spacings in each array configuration.

Table 3
Fits to Periodic Modulation of LAT Light Curve of 4FGL J1702.7−5655

Parameter	Part 1	Part 2
Flux Outside Eclipse ($F_{\rm unecl}$)	4.53 ± 0.03	4.56 ± 0.02
Flux in Eclipse ($F_{\rm ecl}$)	3.91 ± 0.22	3.85 ± 0.15
Eclipse Center (MJD)	57000.168 ± 0.004	57000.181 ± 0.002
Eclipse Minimum Full Duration (Δ)	0.044 ± 0.038	0.021 ± 0.027
Eclipse Ingress Start ($\phi_{\rm ing}$)	0.940 ± 0.033	0.923 ± 0.021
Eclipse Egress End ($\phi_{\rm egr}$)	0.050 ± 0.019	0.055 ± 0.017
Eclipse Total Duration (Egress - Ingress) (ϕ)	*0.110 ± 0.038*	*0.132 ± 0.027*
Derived Ingress Duration (ϕ)	*0.038 ± 0.038*	*0.066 ± 0.024*
Derived Egress Duration (ϕ)	*0.028 ± 0.027*	*0.044 ± 0.022*
Sine Wave Half-Amplitude	—	0.127 ± 0.034
Sine Wave Maximum (MJD)	—	57000.293 ± 0.009
Sine Wave Maximum[1] (ϕ)	—	*0.51 ± 0.04*
Sine Wave Maximum[2] (ϕ)	—	*0.46 ± 0.04*
Period (d)	*0.2438034*	*0.2438034*

Note. — Fits were made to the probability-weighted aperture photometry light curve with 100 s time bins. Phase 0 corresponds to the center of the full eclipse. Parameters in italics are derived from the other parameters which were fitted. The orbital period was held fixed at the value determined from the power spectrum. Fluxes are in units of p.ph$\times 10^{-8}$ cm^{-2} s^{-1}. [1]Relative to the Part 1 eclipse center. [2]Relative to the Part 2 eclipse center. Fits are plotted in Fig. 4.

Table 4
Fits to Binary-Phase Resolved LAT Light Curve of
4FGL J1702.7−5655

Parameter	Part 1	Part 2
Flux Outside Eclipse ($F_{\rm unecl}$)	3.92 ± 0.16	4.04 ± 0.12
Flux in Eclipse ($F_{\rm ecl}$)	0.89 ± 0.48	0.96 ± 0.44
Sine Wave Half-Amplitude	—	0.70 ± 0.18
Sine Wave Maximum (MJD)	—	*57000.296 ± 0.009*
Sine Wave Maximum[1] (ϕ)	—	0.52 ± 0.04
Sine Wave Maximum[2] *(ϕ)*	—	*0.47 ± 0.04*
Period (d)	*0.2438034*	*0.2438034*

Note. — Fits were made to the phase-resolved fluxes obtained from likelihood analysis. Eclipse parameters, excluding flux, were held fixed at the values obtained from fitting the aperture-photometry light curve given in Table 3. Parameters in italics are derived from the other parameters which were fitted. Fluxes are in units of ph$\times10^{-8}$ cm^{-2} s^{-1}. [1]Relative to the Part 1 eclipse center. [2]Relative to the Part 2 eclipse center. The fits are plotted in Fig. 8.

Table 5
Selected Binary Millisecond Pulsars

Name	Photon Flux (ph $cm^{-2} s^{-1} \times 10^{-10}$)	Energy Flux (erg $cm^{-2} s^{-1} \times 10^{-12}$)	Orbital Period (days)	Pulse Period (ms)	Eclipse?	Sine?
4FGL J1702.7−5655	31.68 ± 1.10	29.09± 1.43	0.2438033	?	Y	Y/I(?)
4FGL J1048.6+2340 (PSR J1048+2339)	6.38 ± 0.53	5.07 ± 0.49	0.2505191 (a)	4.67	Y	N
4FGL J1816.5+4510 (PSR J1816+4510)	16.91 ± 0.74	10.18 ± 0.52	0.3608934817 (b)	3.19	Y	N
4FGL J0427.8−6704	6.57 ± 0.43	8.57 ± 0.49	0.3667200 (c)	?	Y	N
4FGL J1959.5+2048 (PSR B1957+20)	23.29 ± 1.1	16.07 ± 0.89	0.38196661 (d)	1.61	Y	Y/S
4FGL J2129.8−0428 (PSR J2129-0429)	11.51± 0.72	6.68 ± 0.49	0.63522741310 (e)	7.61	Y	N
4FGL J1311.7−3430 (PSR J1311−3430)	75.68 ± 1.50	60.97 ± 1.26	0.0651157347 (f)	2.56	N	Y/I
4FGL J2241.7−5236 (PSR J2241−5236)	46.82 ± 1.37	25.37 ± 1.11	0.1456722372 (g)	2.19	N	Y/S
4FGL J2339.6−0533 (PSR J2339−0533)	47.02 ± 1.26	29.16 ± 0.84	0.19309790 (h)	2.88	N	Y/S
4FGL J2039.5−5617 (PSR J2039−5617)	21.83 ± 0.83	15.13 ± 0.67	0.227979805 (i)	2.65	N	Y/S
4FGL J1228.0−4853 (PSR J1227−4853)	24.80 ± 1.08	22.58 ± 1.26	0.287887802 (j)	1.69	N	Y/S*

Note. — Photon flux is for the energy range 1 - 100 GeV, energy flux is for the range 100 MeV to 100 GeV. Both are taken from the 4FGL DR2 catalog (v27). The "Eclipse" column indicates whether an eclipse has been reported in LAT observations. The "Sine" column indicates whether quasi-sinusoidal modulation in gamma-rays has been reported, where "S" and "I" indicate orbital maximum is nearest superior or inferior conjunction of the compact object. * For 4FGL J1228.0−4853 an orbital maximum was reported near inferior conjunction by Xing & Wang (2015) while An (2022) reported a minimum near that phase from a longer dataset. References: (a) Deneva et al. (2016), (b) Stovall et al. (2014), (c) Kennedy et al. (2020), (d) Arzoumanian et al. (1994), (e) Kong et al. (2018), (f) An et al. (2017), (g) An et al. (2018), (h) Romani & Shaw (2011), (i) Clark et al. (2021a), (j) de Martino et al. (2020). The orbital period for 4FGL J1702.7−5655 is from this work.